Journal of Electroceramics, 13, 683–689, 2004

Characterization of Pr- and Sm-Doped $Ce_{0.8}Gd_{0.2}O_{2-\delta}$

R. TORRENS[1], N.M. SAMMES[2] & G. TOMPSETT[3]

[1]*Department of Materials and Process Engineering, University of Waikato, Private Bag 3105, Hamilton, New Zealand*
[2]*Department of Mechanical Engineering, University of Connecticut, 191 Auditorium Road, Storrs, CT 06269-3139, USA*
[3]*Department of Chemical Engineering, University of Massachusetts, 159 Goessmann Lab, Amherst, MA 01003, USA*

Submitted February 25, 2003; Revised June 11, 2003; Accepted June 12, 2003

Abstract. $Ce_{0.8}Gd_{0.2-y}Pr_yO_{2-\delta}$ ($y = 0$–0.05) and $Ce_{0.8}Gd_{0.2-y}Sm_yO_{2-\delta}$ ($y = 0$–0.05) SOFC electrolyte materials were prepared using a reverse-strike co-precipitation method. The resulting powders were characterized using X-ray diffraction, Raman spectroscopy and electrochemical methods. XRD confirmed a single fluorite phase for all compositions. Increased Pr and Sm dopant level was found to cause a shift in the peak positions to slightly higher d-spacings with respect to pure CeO_2. The experimental lattice parameter was calculated using the peak positions determined from the XRD patterns. Raman spectra, for all dopant levels, showed two distinctive band features, namely a band at ca. 460 cm^{-1} and a broader, weaker band at ca. 570 cm^{-1}. As the proportion of praseodymia dopant is increased, the oxygen vacancy band shifts to a slightly lower wavenumber and decreases in relative intensity to the F_{2g} band. However, an anomaly occurs at the 1% dopant level; the oxygen vacancy band having a very low relative intensity. The conductivity was determined using AC—impedance spectroscopy, and it was found that for praseodymia, a maximum is observed at $y = 0.015$, while for samaria the maximum is observed at $y = 0.01$. It is also observed that the ionic conductivity for the samaria doped samples are lower than those of the praseodymia doped samples.

Keywords: $Ce_{0.8}Gd_{0.2-y}Pr_yO_{2-\delta}$ and $Ce_{0.8}Gd_{0.2-y}Sm_yO_{2-\delta}$ electrolytes, X-ray diffraction, Raman spectroscopy, AC impedance

Introduction

Stabilized zirconia has been the traditional solid electrolyte material used for high temperature solid oxide fuel cells (SOFC); operational temperature for yttria stabilized zirconia is typically 1000°C, having an ionic conductivity of approximately 0.1 S/cm [1]. In order to achieve higher SOFC power densities and better longevity through lower operating temperatures, alternative electrolyte materials are under investigation. To date doped ceria electrolytes have shown promise as new intermediate temperature electrolyte materials. Doped ceria electrolytes have been reported as having much higher ionic conductivities than stabilized zirconia [2–5]. Substitution of the Ce^{4+} cation with aliovalent cations results in the incorporation of oxygen vacancies for charge compensation in the lattice structure. CeO_2-Sm_2O_3, [2, 6] CeO_2-Gd_2O_3 [3–5] and CeO_2-Gd_2O_3-Pr_6O_{11} [4,7], for example, have been examined and have shown to have excellent potential as electrolytes in SOFCs. Maricle et al. [4] studied the effect of the addition of praseodymia to gadolinia doped ceria in order to extend the ionic domain boundary. The authors found that the ionic conductivity was enhanced, and the oxygen partial pressure below which *n*-type conductivity became significant was lowered by two orders of magnitude with respect to gadolinia doped ceria. Lubke and Wiemhofer [8] also investigated the effect of praseodymia in CeO_2-Gd_2O_3(CGO), and again found an increase in the overall ionic conductivity. It was found that the addition of Pr increased the grain boundary conductivity and hence the overall ionic conductivity and that this increase was postulated as being due to the reduction of dopant segregation at the grain boundaries.

Huang et al. [9]. also investigated the effect of praseodymia doped CeO_2-Sm_2O_3 (CSO), which at equivalent dopant levels is equal to or possibly superior

to CGO [10]. The authors found that an increase in the conductivity occurred with praseodymia doping, due to an increase in the electronic conductivity, while the ionic conductivity remained unchanged. Further, the work by Shuk and Greenblatt [11] on praseodymia doped ceria showed that while the addition of praseodymia increased the ionic conductivity, there was still significant electronic conductivity. This was expected as it is known that praseodymia exhibits mixed valency [12] at atmospheric pressure, and hence an equilibrium would exist based on the oxygen partial pressure. Steele [13] commented on the results of Huang et al. [9], and questioned whether the addition of the praseodymia to high purity gadolinia doped ceria gave any benefit, since grain boundary conductivity is influenced by impurities, fabrication method and processing variables. Thus, praseodymia potentially influences the grain boundary conductivity of the materials which in turn may be affected by the differences in impurity levels and fabrication methods. Raman spectroscopy has been used to investigate the structure of undoped and doped ceria materials, giving information of the phase and the defect chemistry of the material. For example McBride et al. [14] studied rare earth doped ceria using Raman spectroscopy. For the fluorite symmetry a single Raman allowed mode (F_{2g}) is observed. For pure ceria, this mode occurs at ca. 465 cm^{-1} while it is observed to shift to lower wavenumbers with doping as shown in Table 1. Table 1 summarizes the Raman band positions of the F_{2g} and defect induced bands observed for undoped and doped-ceria materials. Secondary bands at ca. 500–600 cm^{-1} have been attributed to defect induced Raman shifts, namely due to the oxygen defects [15]. For Y^{3+} doped ceria, four type of oxygen defects have been assigned [15] to the fluorite lattice. These may induce Raman shifts in the spectrum of yttria doped ceria.

Table 1. Raman band positions for undoped and doped ceria.

Composition	F_{2g} band position (cm^{-1})	Defect induced Raman bands (cm^{-1})	Ref.
CeO_2	468		[15]
CeO_2	465		[15]
$Ce_{0.95}Gd_{0.05}O_{2-x}$	460	555, 595 ($V_{\ddot{O}}$)	[15]
$Ce_{0.90}Gd_{0.10}O_{2-x}$	460	549, 592 ($V_{\ddot{O}}$)	[15]
$Ce_{0.85}Gd_{0.15}O_{2-x}$	460	545, 593 ($V_{\ddot{O}}$)	[15]
$Ce_{0.80}Gd_{0.20}O_{2-x}$	462	539, 594 ($V_{\ddot{O}}$)	[15]
$Ce_{0.96}Y_{0.04}O_{2-x}$	ca. 460	540, 610 ($V_{\ddot{O}}$)	[15]
$Ce_{0.82}Y_{0.18}O_{2-x}$	ca. 460	540, 610 ($V_{\ddot{O}}$)	[15]
$Ce_{0.96}La_{0.04}O_{2-x}$	ca. 460	540, 600 ($V_{\ddot{O}}$)	[15]
$Ce_{0.96}Zr_{0.04}O_{2-x}$	ca. 460	590 ($V_{\ddot{O}}$)	[15]
$Ce_{0.80}Pr_{0.20}O_{2-x}$	458.6	570 ($V_{\ddot{O}}$)	[14]
$Ce_{0.90}Tb_{0.10}O_{2-x}$	462.1		[14]
$Ce_{0.85}Gd_{0.15}O_{2-x}$	464.2		[14]
$Ce_{0.90}Eu_{0.10}O_{2-x}$	464.5		[14]
$Ce_{0.80}Nd_{0.20}O_{2-x}$	461.8		[14]
$Ce_{0.80}La_{0.20}O_{2-x}$	458.5	550 ($V_{\ddot{O}}$)	[14]
$Ce_{0.80}Sm_{0.20}O_{2-x}$	ca. 460	540-600 ($V_{\ddot{O}}$)	[16]

Moreover, Mineshige et al. [16] observed an increase in the relative intensity of the oxygen vacancy bands, in the range 540–600 cm^{-1}, for $Ce_{0.8}Sm_{0.2}O_{2-\delta}$, with decrease in oxygen partial pressure. There is a direct relationship between the vacancy band area and the oxygen partial pressure,upon annealing; these results are also summarized in Table 1.

In this present study we will examine the affect on the structure and conductivity of $Ce_{0.8}Gd_{0.2}O_{2-\delta}$by double doping with praseodymia and samaria, using X-ray diffraction, Raman spectroscopy and ac-impedance spectroscopy.

Experimental

$Ce_{0.8}Gd_{0.2-y}Pr_yO_{2-\delta}$ ($y = 0$–0.05) and $Ce_{0.8}Gd_{0.2-y}$-$Sm_yO_{2-\delta}$ ($y = 0$–0.05) powders were synthesized using a reverse-strike co-precipitation method, as described by Van herle et al. [17]. Stoichiometric quantities of the required metal nitrates (Aldrich all greater than 99.9% pure) were dissolved in distilled water and stirred to form an aqueous solution of 1 M total metal ion concentration. The nitrate solution was added drop-wise to 0.06 M oxalic acid (adjusted to pH 6.7–6.9 using ammonia solution). The precipitant was maintained in the pH range of 6.7–6.9 by addition of further ammonia solution during the nitrate addition. The resultant precipitate was filtered, washed with de-ionized water and isoproponal, and finally oven dried.

Calcination was performed at 700°C for 1 h followed by uniaxial pressing at 14 MPa to form a pellet (14 mm diameter) and wet-bag isostatic pressing at 200 MPa. 3 wt% oleic acid was added to the powder, using a milling process for 12 h, to increase the green compact strength of the pellet.

Sintering was undertaken at 1300–1600°C for 2–10 h. All samples had percentage theoretical densities greater than 96%, as observed using the standard Archimedes method. All measurements were performed on samples after equilibrating in air at 1200°C

for 2 h. Powder X-ray diffraction was performed on the samples using a Philips X'Pert diffractometer using Cu K_α radiation. Philips analytical software was used for instrument control and data acquisition. Peak positions were determined from fitted profiles obtained using Philips ProFit software. Crystallite size measurements were performed using the (400) peak, a step size of 0.005°2Θ, and a scan time of 1.25 seconds per step. The software obtained half width values from which the crystallite size was calculated. Lattice parameters were determined from the peak positions in the XRD patterns and refined using UnitCell software. High temperature XRD measurements from 500–1000°C were performed using a high temperature camera (HTK-16 Anton-Paar) fitted to the Philips X'Pert XRD.A platinum strip heating filament was used equipped with two Pt-Pt10%Rh thermocouples.

Particle size analysis was performed on the powders using a Mastersizer S lazer diffraction system (Malvern Instruments) equipped with a MS17 sampler, using water as the dispersant.

Raman spectroscopy was performed on the sintered pellets using a Raman spectrometer (System 2000 Renshaw), equipped with a microscope stage for analyzing small samples with 180° incident geometry. A 782 nm near infrared laser line, with an 8 mW incident power was employed to excite laser Raman spectra. Spectra were obtained using an uncoated Olympus x50 objective lens with spectra being the average of 5 scans at 60 seconds per scan.

Impedance spectroscopy was performed on the samples using a Solatron 1260 Impedance Gain-Phase analyzer from 0.1 Hz to 10 MHz, with 10 mV AC amplitude applied. Zplot® software was used to control the system, while Zview® program was used to collect and analyze the data. The compacts used in the measurements were coated on both sides with platinum ink and sintered at 1000°C for 1 h. Analysis was performed on the samples as a function of both temperature (between 300–600°C) and oxygen partial pressure. Change in oxygen partial pressure was performed using calibrated N_2/H_2 and H_2/water. Changes in oxygen partial pressure using the H_2/water systems was performed by bubbling hydrogen through a temperature controlled gas bubbler and using heated gas lines to the cell to prevent condensation occurring. Samples were given an 8 h equilibration time between each measurement, and a number of measurements were performed at the same oxygen partial pressure to ensure that equilibrium had occurred.

Results and Discussion

In this work we will use the following terminology; CGP and CGS stand for $Ce_{0.8}Gd_{0.2-y}Pr_yO_{2-\delta}$ and $Ce_{0.8}Gd_{0.2-y}Sm_yO_{2-\delta}$ respectively, while the number stands for the dopant concentration of y (0.005, 0.01, 0.015, 0.03, 0.05 stand for $y = 0.005, 0.01, 0.015, 0.03$ and 0.05 respectively). Thus, CGP03, for example, means $Ce_{0.8}Gd_{0.17}Pr_{0.03}O_{2-\delta}$, while CGS05 means $Ce_{0.8}Gd_{0.15}Sm_{0.05}O_{2-\delta}$.

Figures 1(a)–1(b) shows the room temperature powder X-ray diffraction patterns for $Ce_{0.8}Gd_{0.2-y}Pr_yO_{2-\delta}$

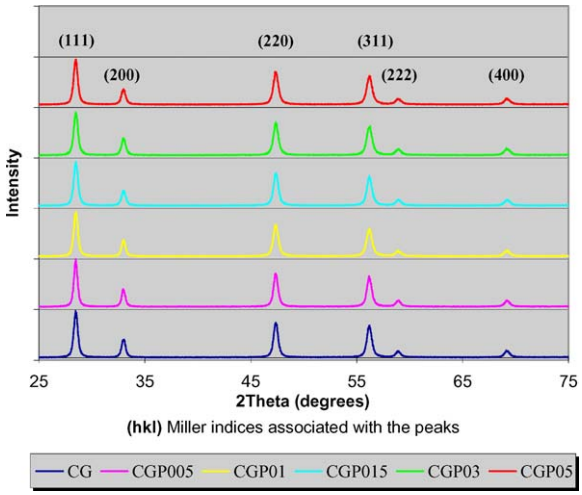

(a)

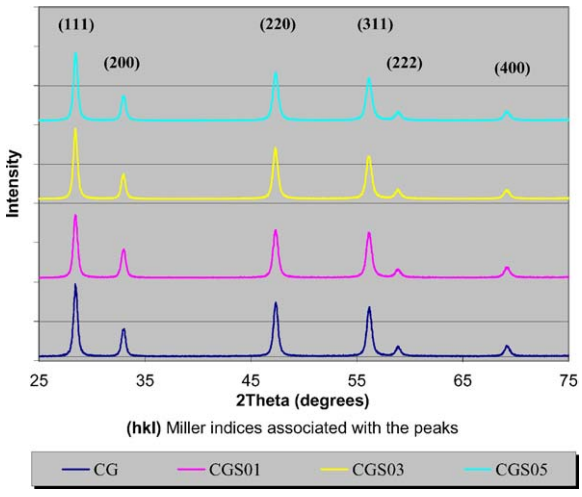

(b)

Fig. 1. (a) Room temperature powder X-ray diffraction patterns for $Ce_{0.8}Gd_{0.2-y}Pr_yO_{2-\delta}$ ($y = 0$–0.05). (b) Room temperature powder X-ray diffraction patterns for $Ce_{0.8}Gd_{0.2-y}Sm_yO_{2-\delta}$ ($y = 0$–0.05).

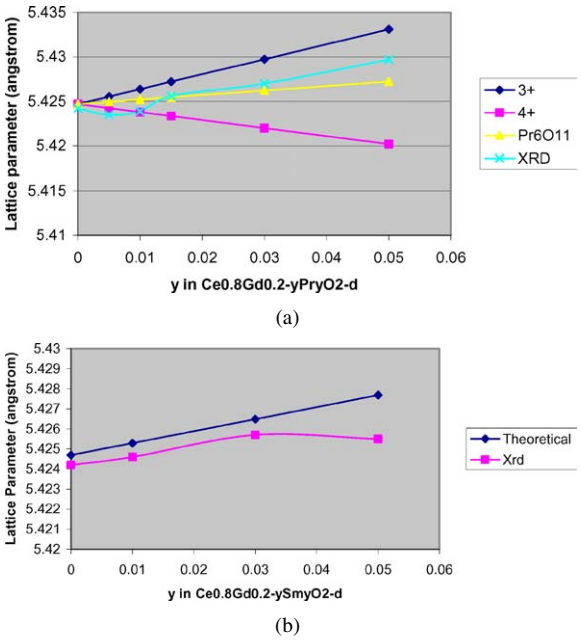

Fig. 2. (a) The effect of lattice parameter on the value of y in $Ce_{0.8}Gd_{0.2-y}Pr_yO_{2-\delta}$. (b) Effect of lattice parameter on the value of y in $Ce_{0.8}Gd_{0.2-y}Sm_yO_{2-\delta}$.

($y = 0$–0.05) and $Ce_{0.8}Gd_{0.2-y}Sm_yO_{2-\delta}$ ($y = 0$–0.05) respectively. The patterns confirm that all the materials were single phase. Increased Pr and Sm dopant level was found to cause a shift of the peak positions to slightly higher d-spacings with respect to pure CeO_2. This was attributable to the dissolution of the dopant species with a larger ionic radii than Ce^{4+} (0.97 Å); the presence of these larger species (Gd^{3+} (1.053 Å), Sm^{3+} (1.097 Å) and the mixed valence species Pr^{4+}/Pr^{3+} (0.96/1.126 Å)) causes expansion of the lattice [18]. Figure 2(a) shows the effect of lattice parameter on the value of y in $Ce_{0.8}Gd_{0.2-y}Pr_yO_{2-\delta}$. The experimental lattice parameter was calculated using the peak positions determined from the XRD patterns of the samples, using Eq. (1), where a is the lattice parameter, x is the dopant concentration, r_m, r_{Ce}, and r_O are the ionic radii of the dopant metal ion (m), Ce^{4+}, and O^{2-} respectively. The effective ionic radius of an oxygen vacancy, r_{vo}, was determined by Hong and Virkar [19] to be 1.164 Å, and represents a contraction compared to the ionic radius of the oxide ion, 1.42 Å.

$$a = \frac{4}{\sqrt{3}} x r_m + (1 - x) r_{Ce} + (1 - 0.25x) r_O + 0.25 x r_{vo} \quad (1)$$

The three theoretical lattice parameter lines are based on calculations assuming Pr to be in the Pr^{3+}, Pr^{4+} or Pr_6O_{11} mixed valence state. It can be seen that the experimental data falls within the range of lattice parameters possible, though does not match any of the theoretical values. The variance in lattice parameter is postulated as being due to the ratio of Pr^{3+} to Pr^{4+}, which, although assumed to be constant, is potentially a variable in this work.

Figure 2(b) shows the effect of lattice parameter on the value of y in $Ce_{0.8}Gd_{0.2-y}Sm_yO_{2-\delta}$. It can be seen that the lattice parameters determined experimentally are lower than the theoretical values, although show a similar trend; again dependant upon the ratio of Pr^{3+} to Pr^{4+}.

Figure 3 shows the Raman spectra of $Ce_{0.8}Gd_{0.2-y}Pr_yO_{2-\delta}$, $y = 0.005$–0.05. Spectra for all dopant levels show two distinctive band features, namely a band at ca. 460 cm^{-1} and a broader, weaker band at ca. 570 cm^{-1}. This is consistent with the results obtained by McBride et al. [14] for ceria doped with a single rare earth species. McBride et al. [14] found that in addition to the one Raman active mode for the fluorite structure, there was also a new band present in the doped samples when compared to pure ceria. The allowed Raman mode has F_{2g} symmetry and occurs at 465 cm^{-1} in pure ceria. The additional band observed in spectra of doped samples was attributed to oxygen vacancies formed by doping with an aliovalent species [15]. This band was found to occur at a Raman shift of ca. 570 cm^{-1}.

It can be seen that, in general, as the proportion of praseodymia dopant is increased, the oxygen vacancy band shifts to a slightly lower wavenumber and decreases in relative intensity to the F_{2g} band. However, an anomaly occurs at the 1% dopant level; the oxygen vacancy band having a very low relative intensity. This anomaly could be ascribed to an increase in the Pr^{4+} oxidation state. Samples from this powder have shown similar effects in crystallite size determination at this dopant level (1%), as shown in Fig. 4. The decrease in the oxygen vacancy band intensity may be explained by the fact that praseodymia is likely present as a mixed valence species. Therefore substituting the mixed valence Pr^{4+}/Pr^{3+} would decrease the overall amount of M^{3+} present, and hence decrease the number of oxygen vacancies introduced from charge compensation. Alternatively, it could be postulated that at the 1% Pr dopant level a critical size-charge effect occurs between the Pr cation, the Gd cation and the Ce

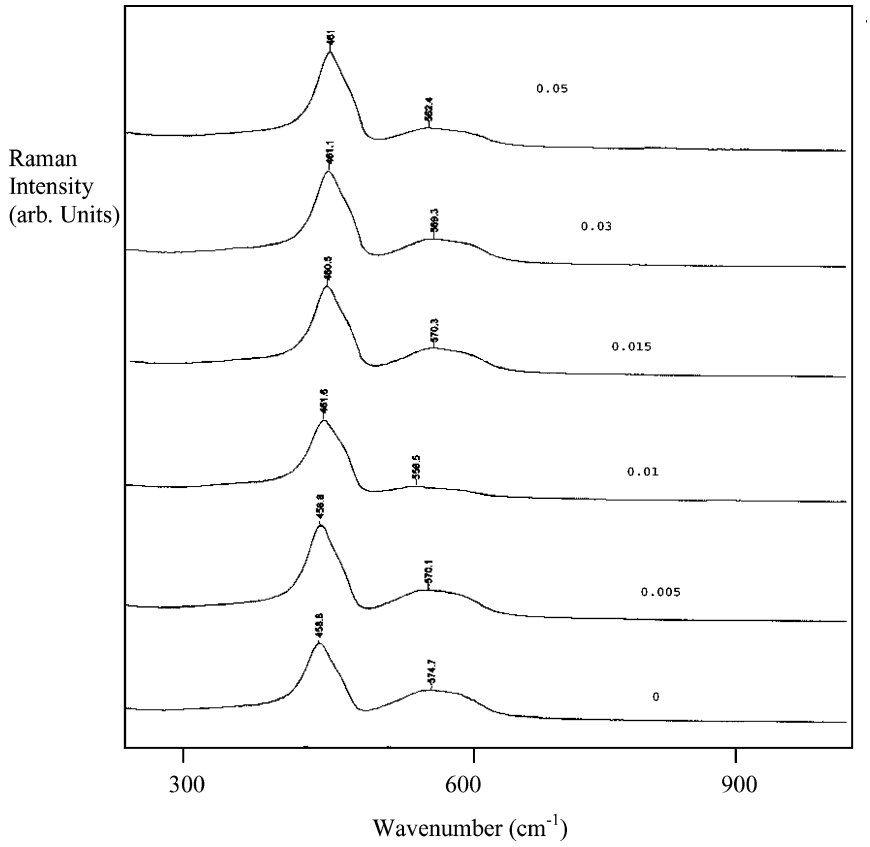

Fig. 3. Raman spectra of $Ce_{0.8}Gd_{0.2-y}Pr_yO_{2-\delta}$, $y = 0.005, 0.01, 0.015, 0.03, 0.05$.

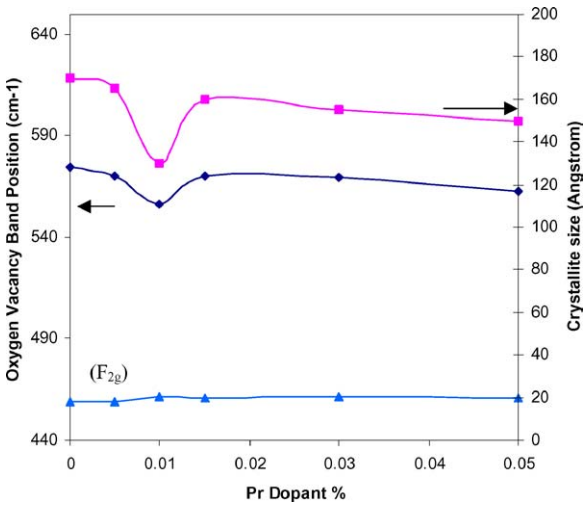

Fig. 4. Graph of oxygen vacancy band position compared to crystallite size with change in Pr dopant percentage.

cation affecting the crystallite size and oxygen vacancy. A shift to lower frequencies for the oxygen vacancy band indicated a vibration associated with a lower energy. It has been observed by Huang et al. [20] that a maxima occurs in the ionic conductivity at a dopant level of ca 1 mol% praseodymia in CSO. This could be postulated as being due to the cation interaction giving rise to a weaker bonding oxygen vacancy site. Huang et al. [20] found that 5 mol% praseodymia doping in CSO gave a maxima in crystallite size. The maxima in ionic conductivity for Sm-doped ceria occurs at 17 mol% Sm, while the maxima in conductivity for gadolinia doped ceria occurs at ca. 20 mol% Gd [21].

It can be seen that the addition of the praseodymia has little effect on the position of the F_{2g} band at ca. 460 cm^{-1}, with only a slight increase at the 1 mol% praseodymia dopant level. It should be noted that this band (and the oxygen vacancy band) appears to be a composite of two bands from the shoulders at ca. 475

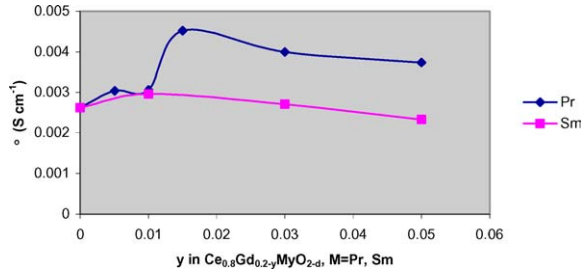

Fig. 5. Isothermal plot of total ionic conductivity versus dopant concentration at 500°C.

and 600 cm^{-1} respectively. The additional shoulder bands have been assigned to the presence of the dopant [22].

Figure 5 shows an isothermal plot of total ionic conductivity versus dopant concentration at 500°C. It can be seen that a maximum in conductivity is obtained for both systems. For praseodymia, this maximum is observed at $y = 0.015$, while for samaria the maximum is observed at $y = 0.01$. It is also observed that the ionic conductivity for the samaria doped samples is lower than those of the praseodymia doped samples. At low temperatures (300°C) it is possible to resolve the individual lattice and grain boundary components of the overall conductivity, as clearly resolved arcs are present in the complex plane impedance plots. The resulting values of grain boundary and lattice conductivity are displayed in Fig. 6(a). It can be seen that the addition of Pr has an effect on both the lattice and grain boundary conductivities, with the grain boundary conductivity affected more than the lattice. There is an anomalous conductivity measured for the 10%Pr (sample) grain boundary conductivity, indicating that at this composition the Pr doping has a critical effect on the grain boundaries. This result is in agreement with Steele [13], namely, that with increase in Pr doping, there is an increase in the grain boundary conductivities. However, there is also an increase in the intrinsic conductivity of the materials with Pr doping.

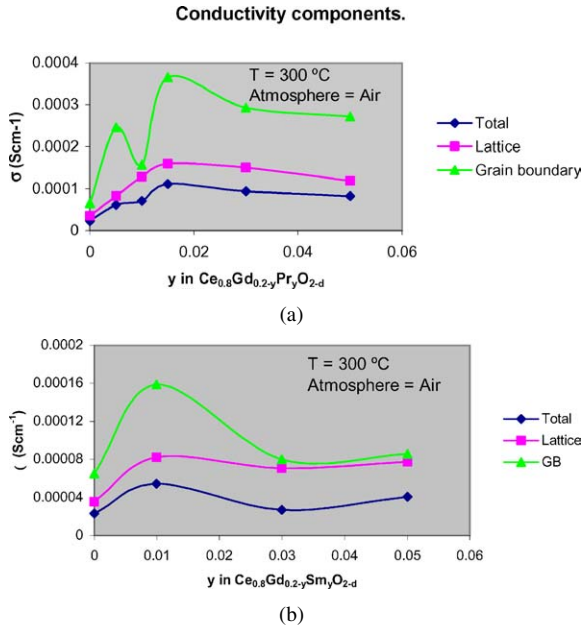

Fig. 6. (a) Conductivity components of $Ce_{0.8}Gd_{0.2-y}Pr_yO_{2-\delta}$, $y = 0$–0.05. (b) Conductivity components of $Ce_{0.8}Gd_{0.2-y}Sm_yO_{2-\delta}$, $y = 0$–0.05.

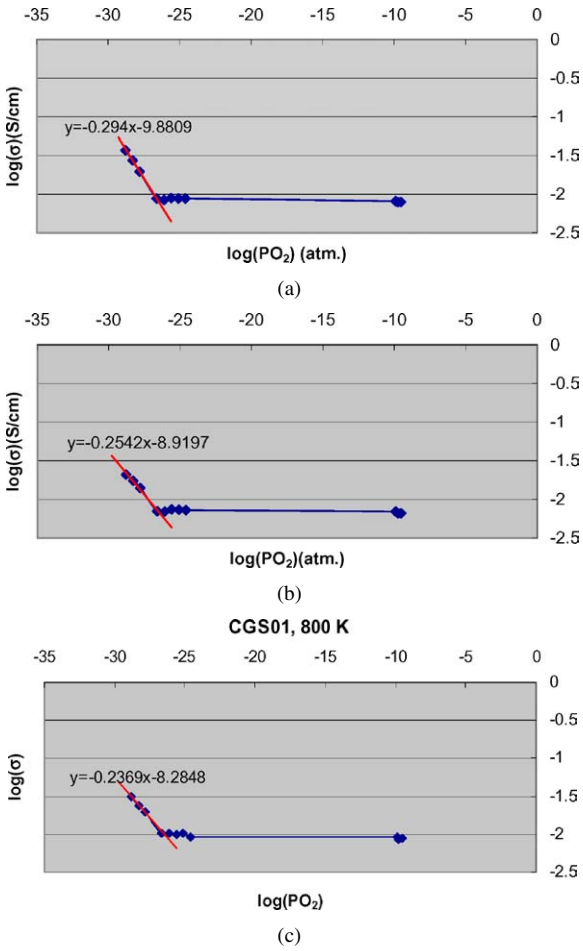

Fig. 7. (a) Effect of oxygen partial pressure on the total conductivity of ceria-gadolinia, at 800 K. (b) Effect of oxygen partial pressure on the total conductivity of CGPO15, at 800 K. (c) Effect of oxygen partial pressure on the total conductivity of CGSO15, at 800 K.

Similar results were observed for the samaria doped samples, as shown in Fig. 6(b). It can be seen that at the 10%Sm doping level, there is a significant increase in the grain boundary conductivity. For doubly doped CGO with Pr and Sm, at the 10% dopant level, a critical structural effect occurs affecting the crystallite size and the grain boundary conductivity.

Figures 7(a)–(c) show the effect of oxygen partial pressure on the total conductivity of CGO, CGPO15 and CGSO15, respectively. What is quite apparent is that there appears to be no discernible effect on the ionic domain boundary (towards *n*-type conductivity) with oxygen partial pressure, as was observed by Maricle et al. [3]. This was the case for both praseodymia and samaria doped systems, at all levels of doping. Thus it is quite apparent that the only effect of doping is on the ionic conductivity,

Conclusions

1. $Ce_{0.8}Gd_{0.2-y}Pr_yO_{2-\delta}$ ($y = 0$–0.05) and $Ce_{0.8}Gd_{0.2-y}Sm_yO_{2-\delta}$ ($y = 0$–0.05) electrolyte materials were prepared using the reverse-strike co-precipitation method. XRD confirmed a single fluorite phase for all compositions.
2. Increased Pr and Sm dopant levels was found to cause a shift of the XRD peak positions to slightly higher d-spacings with respect to pure CeO_2. The experimental lattice parameter was calculated using the peak positions determined from the XRD patterns.
3. Raman spectra for all dopant levels show two distinctive band features, namely a band at ca. 460 cm^{-1} and a broader, weaker band at ca. 570 cm^{-1}. As the proportion of praseodymia dopant is increased, the oxygen vacancy band shifts to a slightly lower wavenumber and decreases in relative intensity to the F_{2g} band. However, an anomaly occurs at the 1% dopant level; the oxygen vacancy band having a very low relative intensity.
4. The conductivity was determined using AC–impedance, and it was found that for praseodymia doped CGO, a maximum is observed at $y = 0.015$, while for samaria doped, the maximum is observed at $y = 0.01$. It is also observed that the ionic conductivity for the samaria doped samples are lower than those of the praseodymia doped samples. At 10% Pr dopant, a decrease in the grain boundary conductivity is observed, however, a maxima in grain boundary conductivity occurs for the Sm doped samples.

References

1. B.C.H. Steele, in *Science and Technology of Zirconia V*, edited by S.P.S. Badwal, M.J. Bannister and R.H.J. Hannink (Technomic Publishing Co. Inc., Pennsylvania, 1993), p. 713.
2. C.C. Chen, M.M. Nasrallah, and H.U. Anderson, *J. Electrochem. Soc.*, **140**, 3555 (1993).
3. H. Yahiro, K. Eguchi, and H. Arai, *Solid State Ionics*, **36**, 71 (1989).
4. D.L. Maricle, T.E. Swarr, and S. Karavolis, *Solid State Ionics*, **52**, 173 (1992).
5. Z. Tianshu, P.Hing, H.Huang, and J. Kilner, *Solid State Ionics*, **148**, 567 (2002).
6. T. Inoue, T. Setoguchi, K. Eguchi, and H. Arai, *Solid State Ionics*, **35**, 285 (1989).
7. L. Navarro, F. Marques, and J. Frade, *J. Electrochem. Soc.*, **1444**, 267 (1997).
8. S. Lubke and H.D Wiemhofer, *Solid State Ionics*, **117**, 229 (1999).
9. W. Huang, P. Shuk, and M. Greenblatt, *Solid State Ionics*, **113–115**, 305, (1998).
10. H. Yahiro, Y. Eguchi, K. Eguchi, and H. Arai, *J. Appl. Electrochem.*, **18**, 527 (1988).
11. P. Shuk and M. Greenblatt, *Solid State Ionics*, **116**, 217 (1999).
12. H. Inaba and K. Naito, *Solid State Ionics*, **50**, 100 (1983).
13. B.C.H. Steele, *Solid State Ionics*, **129**, 95 (2000).
14. J.R. McBride, K.C. Hass, B.D. Poindexter, and W.H. Weber, *J. Appl. Phys.*, **76**(4), 2435 (1994).
15. Nakajima, A. Yoshihara, and M. Ishigame, *Phys. Rev. B.*, **50**(18), 13297 (1994).
16. Mineshige, T. Taji, Y. Mori, M. Kobune, S. Fujii, N. Nishi, M. Inaba, and Z. Ogumi, *Solid State Ionics*, **135**, 481 (2000).
17. J. Van Herle, T. Kawada, W. Sakai, H. Yokokawa, and M. Dokiya, in *Solid Oxide Fuel Cells IV*, edited by M. Dokiya, H. Tagawa, O. Yamamoto, and S.C. Singhal. (Electrochemical Society, Pennington, New Jersey, 1995), p. 1082.
18. R.D. Shannon, *Acta Crystallogr., Sect.* A**32**, 751 (1976)
19. S.J. Hong and A.V. Virkar, *J. Am. Ceram. Soc.*, **78**(2) 433 (1995).
20. W. Huang, P. Shuk, and M. Greenblatt, *Solid State Ionics*, **113–115**, 305 (1998).
21. Z. Tianshu, P. Hing, H. Huang, and J. Kilner, *Solid State Ionics* **148**, 567 (2002).
22. N. Sammes, G. Tompsett, Y. Zhang, A. Cartner, and R. Torrens, *Denki Kagaku*, **64**, 674 (1996).